Recovering a thin dipping conductor with 3D electromagnetic inversion over the Caber deposit

Michael S. McMillan, Christoph Schwarzbach, Douglas W. Oldenburg and Eldad Haber, Geophysical Inversion Facility, University of British Columbia, Elliot Holtham, Computational Geosciences Inc., Alexander Prikhodko, Geotech Ltd.*

SUMMARY

Airborne time-domain electromagnetic (EM) data were collected in 2012 over the Caber volcanogenic massive sulfide (VMS) deposit in western Quebec. We inverted the data in three-dimensions (3D) to produce a conductivity inversion model that helped image the thin dipping conductor and surrounding geology. The 3D inversion method consisted of a two-step approach. The first step employed a parametric inversion to recover a best-fitting shape of the dipping conductor using only data exhibiting an anomalous response over the deposit. With the parametric result as an initial and reference model, the second step used a conventional 3D EM inversion with data locations over the entire survey area. The second stage allowed for fine tuning of the shape and conductivity of the central dipping anomaly, while filling in features, such as overburden, in the remaining areas of the domain. The shape of the central conductive anomaly in the 3D inversion compared well with the known outline of the Caber deposit, based on geologic knowledge from past drilling. The overburden layer in the inversion model also agreed with previous geologic mapping. Preliminary results from this two-stage process show that it possible to recover a thin, dipping conductor with sharp boundaries through 3D EM inversion, which has been a difficult challenge in recent years.

INTRODUCTION

Since 2003, many airborne time-domain EM surveys have been collected over the Caber deposit in an effort to image the conductivity signature of the area (Legault et al., 2010). Contrasts in electrical conductivity help distinguish between different rock types and can highlight geologic structures and mineralized zones. This paper focuses on imaging the conductive and steeply dipping Caber deposit with 3D inversion of airborne electromagnetic data. The work builds upon previous research by Legault et al. (2010), that shows plate modeling results over the Caber deposit with older EM data sets.

CABER GEOLOGY

The Caber VMS deposit is a zinc and copper rich ore body located in western Quebec, Canada. Within the Superior Province, the region is part of the Matagami camp of the Abitibi Greenstone Belt (Carr et al., 2008). Locally, the large McIvor fault separates the Caber deposit along with accompanying gabbros, rhyolites and basalts from a granodiorite unit to the north-east (R. Adair, 2011, Zorayda Consulting Ltd. Technical Report), as shown in Figure 1. According to Legault et al. (2010) there is also a layer of thin conductive overburden above the ore-body that thickens to the north-east. The deposit itself is cigar-like in shape with a steep dip of 75 to 85 degrees to the south-west, with a strike direction of 125 degrees. A cross-section through the deposit is shown in Figure 2, which illustrates the thin overburden and the near-vertical nature of the deposit. Steeply dipping rhyolite and gabbro units are also seen in Figure 2 close to sulfide mineralization. The thin, buried nature of the Caber deposit, coupled with its position below conductive overburden makes it a difficult target to detect with airborne electromagnetics. Fortunately, most of the large surrounding units have a more resistive signature compared to the sulfide deposit, making it a feasible, albeit difficult, target.

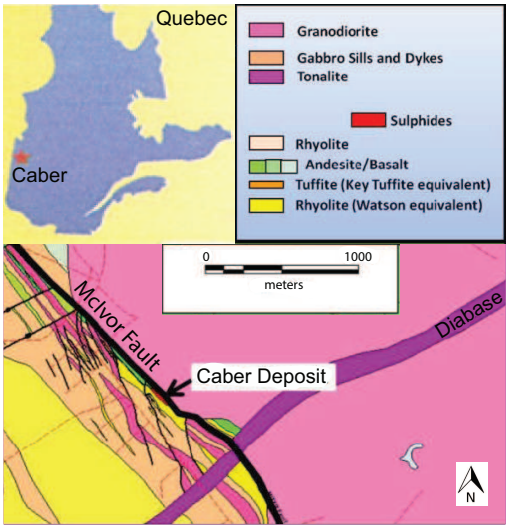

Figure 1: Caber location and regional geology (modified from Legault et al. 2010 and R. Adair 2011 Technical Report)

TIME-DOMAIN AIRBORNE EM

Eight lines of airborne EM were collected over the Caber deposit in 2012 with the Versatile Time-Domain Electromagnetic System (VTEM-35), in an attempt to improve the mapped extent of the thin conductive target. The system, with a loop diameter of 35 m and a dipole moment of 1,300,000 Am^2, acquired z and x-component $\frac{d\mathbf{B}}{dt}$ and $\mathbf{B}$-field measurements, where $\mathbf{B}$ is magnetic flux. A further description of VTEM systems can be found in Allard (2007). The flight lines were spaced 50 m apart with a heading of 225 degrees, and time channels were recorded between 20 μs and 9000 μs. Figure 3 shows a plan map with flight line locations and a best fitting decay parameter tau, calculated from the latest response at each station. The central portion of Figure 3, over the Caber deposit, contains elevated tau values, indicating a relatively conductive

DOI http://dx.doi.org/10.1190/segam2014-0536.1

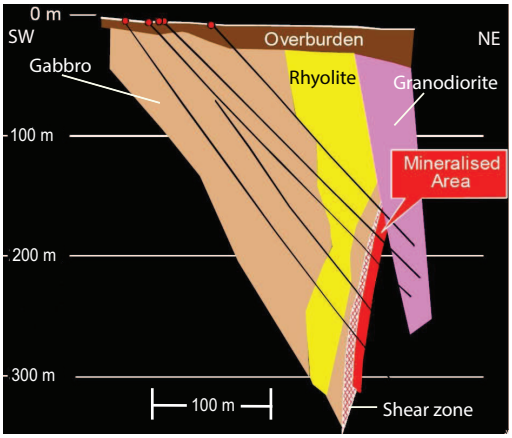

Figure 2: Simplified cross-section through the Caber deposit (modified from Legault et al. 2010)

response of the target. A nearby shear zone, shown in Figure 2, may contribute to this effect, but for simplicity the mineralized area and shear zone will be treated as one response. Elsewhere, the tau values are generally higher in the north-east compared to the south-west, which is consistent with thicker conductive overburden to the north-east. The only exception is a small conductive response in the south-west corner of Figure 3.

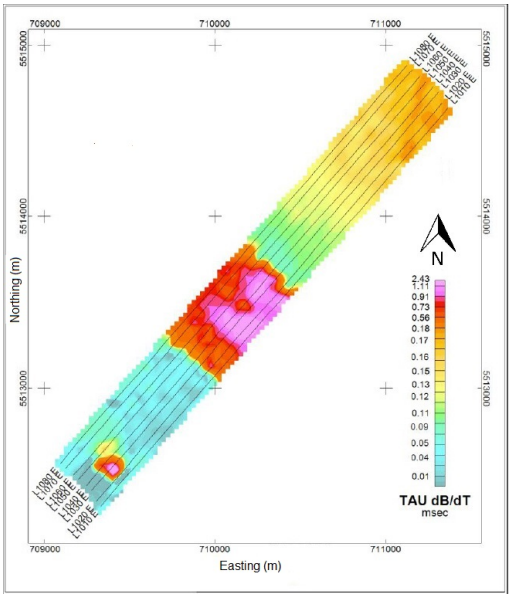

Figure 3: Airborne EM flight lines over the Caber deposit, overlaid on tau-map. The large double-peaked anomaly in the center is indicative of the target.

PLATE MODELING

Best fitting 3D rectangular plates were modeled in the software program Maxwell, developed by ElectroMagnetic Imaging Technology, to match the observed data over the Caber deposit. Five lines with the highest responses over the anomaly were selected using ten time channels between 1247 μs to 4987 μs. Figure 4 shows the best-fitting plate modeling results from line 1040. Figure 4a displays the comparison between $\frac{d\mathbf{B}z}{dt}$ observed data in black, and the predicted data from a best fitting plate in red, while Figure 4b makes the same comparison with $\frac{d\mathbf{B}x}{dt}$ data. The best-fitting plate is illustrated in Figure 4c in blue, overlaid on a resistivity depth image using the transformation scheme from Meju (1998), with depth calibration based on a series of forward models. The recovered plate has a conductivity of 7.25 S/m, and dimensions of 315 m in strike length, 100 m in depth, and 29.5 m in thickness. The modeled conductor dips with a near-vertical angle of 86.5 degrees in a south-west dip direction of 220 degrees. Overall there is a close agreement between observed and predicted data in both components. This signifies that a single dipping plate approximation is appropriate for the observed asymmetric double-peak response in $\frac{d\mathbf{B}z}{dt}$, and the zero-crossing in $\frac{d\mathbf{B}x}{dt}$. The best-fitting plate also matches the geologic cross-section from Figure 2, which adds further confidence to the result. Four other lines produced plate models with similar parameters and they are not shown here.

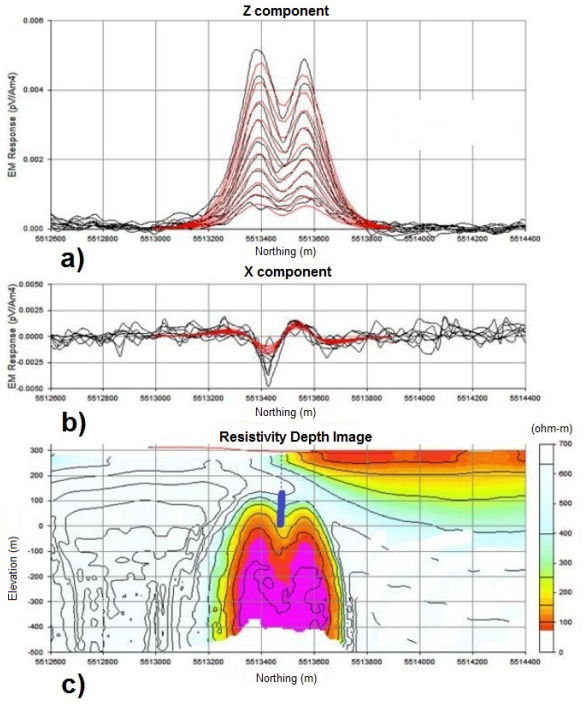

Figure 4: Plate modeling from line 1040. a) $\frac{d\mathbf{B}z}{dt}$ observed data in black with predicted data in red. b) $\frac{d\mathbf{B}x}{dt}$ observed data in black with predicted data in red. c) Best-fitting plate in blue overlaid on resistivity depth image.

3D INVERSION

Finite Volume EM Inversion Theory

Building on encouraging plate modeling results, the data was

DOI http://dx.doi.org/10.1190/segam2014-0536.1

inverted in 3D with TDOcTreeInv from the University of British Columbia (Haber and Schwarzbach, submitted in 2014, *Inverse Problems*). This code, hereafter called a conventional EM inversion, is a regularized algorithm using Gauss-Newton based optimization. It solves quasi-static Maxwell's equations

$$\nabla \times \mathbf{E} + \mu \mathbf{H}_t = 0 \quad (1)$$

$$\nabla \times \mathbf{H} - \sigma \mathbf{E} = \mathbf{s} \quad (2)$$

subject to boundary and initial conditions

$$\mathbf{n} \times \mathbf{E} = 0 \quad (3)$$

$$\mathbf{E}(x,y,z,t=0) = \mathbf{E}_0 \quad (4)$$

$$\mathbf{H}(x,y,z,t=0) = \mathbf{H}_0 \quad (5)$$

in space and time using a finite volume discretization on OcTree meshes (Haber et al., 2007). Here, **E** = electric field vector, **H** = magnetic field vector, μ = magnetic permeability, σ = electrical conductivity, **s** = source vector, **n** = normal vector, x,y,z = spatial coordinates and t = time. Many transmitters are encountered in airborne EM surveys, and they are efficiently handled through direct solvers (Oldenburg et al., 2013; Amestoy et al., 2001; Schenk et al., 2001), which compute a Cholesky decomposition of the forward modeling matrix.

Due to the difficult nature of a thin conductive target beneath conductive overburden, initial 3D inversion models had trouble recovering an appropriate plate-like anomaly. Therefore, a new approach was attempted where a parametric inversion was first performed to recover a best-fitting conductor, and this result was input as the starting and reference model for the conventional 3D inversion. The parametric methodology will be discussed briefly below.

Parametric Inversion Theory

A parametric inversion differs from a conventional method in that it recovers fewer parameters, and an example of a 2D parametric algorithm for direct-current tomography is found in Pidlisecky et al. (2011). In the 3D EM case presented here, a parametric code was written to locate an anomalous body of fixed conductivity in a uniform background. The shape of the anomaly is based on a skewed Gaussian ellipsoid of the form

$$e^{-(\mathbf{x}-\mathbf{x_0})^{\mathbf{T}}\mathbf{M}(\mathbf{x}-\mathbf{x_0})} \quad (6)$$

where **x** is a position vector with spatial x,y,z coordinates, $\mathbf{x_0}$ denotes the center of the ellipsoid, and **M** is a 3×3 symmetric matrix with six unique stretching and skewing parameters m_1 through m_6. An OcTree mesh is used for the inversion, and mesh cells inside the anomalous body are assigned to σ_1, and cells on the outside are assigned to σ_0. Because the conductivity in the model is fixed, the parametric inversion operates with only nine parameters, instead of 275,000 in the conventional 3D inversion. An initial guess is required to start the inversion, and the optimization follows the same Gauss-Newton procedure as the conventional code with a few modifications. These adjustments include removing the regularization term, and scaling all parameters to ensure a well-conditioned Gauss-Newton matrix.

Inversion Results

Eight lines of $\frac{d\mathbf{B}z}{dt}$ data over the central anomaly were inverted using the parametric code, with 102 transmitters and 11 time channels ranging from 505 μs to 2021 μs, on a 20 m $\times$ 20 m $\times$ 20 m OcTree mesh. The initial guess closely approximated the plate model result from Figure 4 with σ_1 = 7.25 S/m and σ_0 = 0.001 S/m, and the inversion terminated after 14 Gauss-Newton iterations. This result was then placed as the initial and reference model for the conventional 3D inversion where the conductivity in each mesh cell could vary. Data from 20 time channels ranging from 167 μs to 2323 μs were included and responses below a threshold of 1e-13 $\frac{V}{Am^2}$ were discarded because of potential noise concerns. In total, 872 transmitter locations from across the entire survey area were inverted. By once again including data over the central anomaly, the conductivity and shape of the parametric result could adjust if needed. Data uncertainties of 5% plus a time-channel dependent noise floor were applied. The noise floor was set to one order of magnitude lower than a 0.001 S/m half-space response. This varying noise floor was chosen to weight each time channel equally in the ensuing result.

The conventional 3D inversion reached convergence after 11 Gauss-Newton iterations, and observed and predicted data plots from two time channels, 167 μs and 505 μs, are illustrated in Figure 5. Overall the two predicted data plots closely resemble the observed data, although there could be some improvement in the south-west corner of Figure 5b, and near the southern portion of the central conductive response in Figure 5d. Holes in the observed and predicted data represent areas of resistive terrain where $\frac{d\mathbf{B}z}{dt}$ responses dropped below 1e-13 $\frac{V}{Am^2}$.

A cross-section through the final inversion model along line 1040 is shown in Figure 6 in resistivity units of Ωm. The view looks to the north-west, and a conductor is clearly imaged, representing the Caber deposit. The anomaly steeply dips to the south-west, and a thin overburden unit thickens to the north-east. The nature of the dip and the overburden corroborates the information from Figure 2 and Figure 4. The sharp boundaries of the dipping conductor are achieved through the parametric inversion, while the conventional EM inversion recovers the overburden, and subtly changes the conductivity and shape of the dipping anomaly. Figure 7a displays a similar view as Figure 6 but with visible mesh cells containing conductivities greater than 0.0057 S/m (less than 175 Ωm). The outline of the plate model from Figure 4 is coloured in white for reference. There is a strong agreement between the 3D inversion and plate modeling results, although the former incorporates data from all eight lines while the plate model represents data from only one line. Figure 7b depicts a final view looking to the north-east with the best-fitting plate from Figure 4 in white. This angle demonstrates that the plate model has a larger strike length and smaller height compared to the 3D inversion outcome, but in general both sets of results correlate well.

Due care must be taken when running this parametric inversion method, because a fixed number of conductors will be produced. In a scenario where two conductive anomalies exist,

DOI http://dx.doi.org/10.1190/segam2014-0536.1

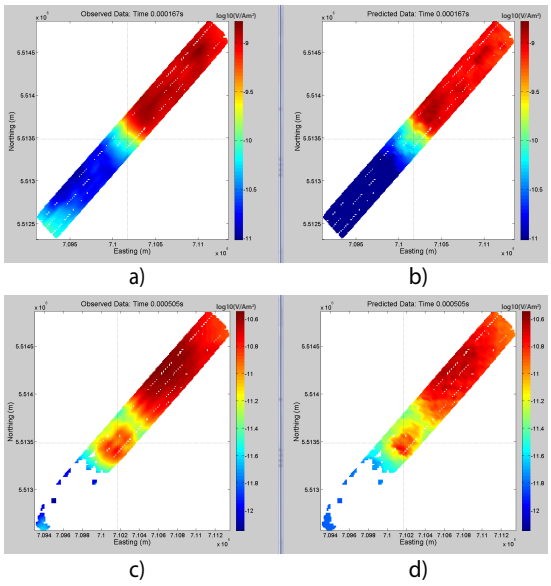

Figure 5: Observed and predicted $\frac{d\mathbf{B}_z}{dt}$ data from the final 3D inversion. The cross-hair is positioned at the center of the conductive anomaly for reference, and data points below a threshold of 1e-13 $\frac{V}{Am^2}$ were removed due to noise concerns. a) Observed data at 167 μs b) Predicted data at 167 μs c) Observed data at 505 μs d) Predicted data at 505 μs.

the response may be modeled erroneously as a single anomaly unless the parametric code is programmed to recover two bodies. Therefore a careful analysis of the observed and predicted data is needed to see whether one or multiple conductive bodies is warranted. In this example, the initial plate modeling suggested that one anomaly was sufficient.

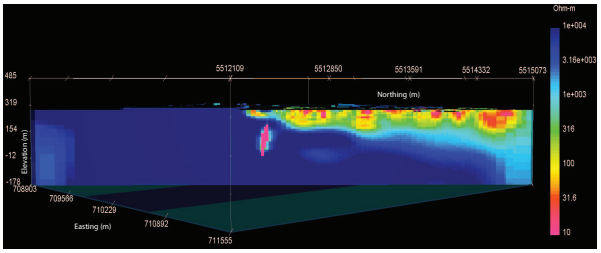

Figure 6: Final 3D inversion showing a cross-section along line 1040 with dipping Caber deposit clearly imaged. The view looks north-west.

CONCLUSIONS AND DISCUSSION

Airborne time-domain EM data (VTEM-35) over the Caber VMS deposit in western Quebec were collected in order to better image the shape of the conductive metal-rich target. Plate modeling demonstrated that a steep south-west dipping plate could fit the $\frac{d\mathbf{B}_x}{dt}$ and $\frac{d\mathbf{B}_z}{dt}$ data on a line-by-line basis. The $\frac{d\mathbf{B}_z}{dt}$ data were then inverted in 3D through a combination of parametric and conventional finite volume EM inverse modeling. The parametric code first imaged a dipping conductor using a selection of data over the conductive target, and subsequently this result was input as the initial and reference model for a conventional 3D EM inversion to recover the remaining features. In total, 102 transmitter sources were included in the local parametric inversion, compared to 872 in the full conventional 3D inversion. The resulting model depicted the Caber deposit as a thin conductor with a steep dip to the south-west, under a small layer of conductive overburden that thickened to the north-east. These observations agreed well with the known geologic information from the area, and from plate modeling.

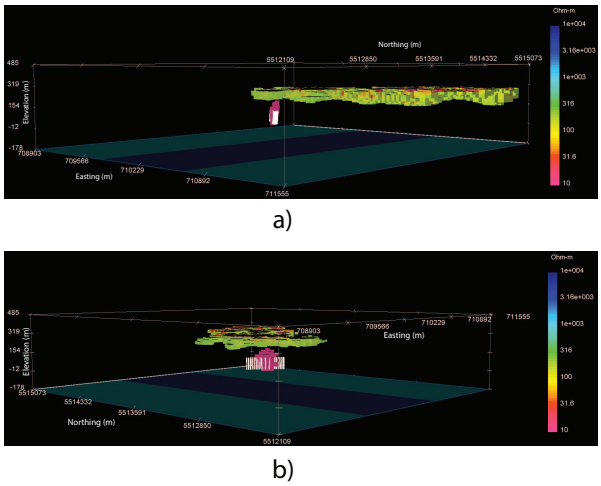

Figure 7: Final 3D inversion showing all cells more conductive than 0.0057 S/m, with the plate model from line 1040 in white. a) The view looks north-west b) The view looks north-east.

One main advantage of the parametric inversion is the ability to recover sharp boundaries, whereas a conventional least-squares inversion preferentially returns a smooth model. These sharp boundaries are seen in the final model, because when conductivity jumps are placed in the reference model of a conventional 3D EM inversion, these discontinuities often remain in the final result. Additional constraints, such as physical properties from drilling, could also be input if desired. Future research will include inverting for the optimal conductivity of the plate and background, as well as incorporating $\frac{d\mathbf{B}_x}{dt}$ data and **B**-field measurements.

ACKNOWLEDGMENTS

The authors thank Geotech Ltd. who provided the data over the Caber deposit and who performed the plate modeling. We also thank members of UBC-GIF for their valued support.

DOI http://dx.doi.org/10.1190/segam2014-0536.1

http://dx.doi.org/10.1190/segam2014-0536.1

EDITED REFERENCES

Note: This reference list is a copy-edited version of the reference list submitted by the author. Reference lists for the 2014 SEG Technical Program Expanded Abstracts have been copy edited so that references provided with the online metadata for each paper will achieve a high degree of linking to cited sources that appear on the Web.

REFERENCES

Allard, M., 2007, On the origin of the HTEM species: Proceedings of the 5th Decennial International Conference on Mineral Exploration, 355–373.

Amestoy, P. R., I. S. Duff, J.-Y. L'Excellent, and J. Koster, 2001, A fully asynchronous multifrontal solver using distributed dynamic scheduling: SIAM Journal on Matrix Analysis and Applications, **23**, no. 1, 15–41, http://dx.doi.org/10.1137/S0895479899358194.

Carr, P. M., L. M. Cathles III, and C. T. Barrie, 2008, On the size and spacing of volcanogenic massive sulfide deposits within a district with application to the Matagami district, Quebec: Economic Geology, **103**, no. 7, 1395–1409, http://dx.doi.org/10.2113/gsecongeo.103.7.1395.

Haber, E., S. Heldmann, and U. Ascher, 2007, Adaptive finite volume method for distributed non-smooth parameter identification: Inverse Problems, **23**, no. 4, 1659–1676, http://dx.doi.org/10.1088/0266-5611/23/4/017.

Legault, J., A. Prikhodko, E. Morrison, A. Bagrianski, P. Kuzmin, and P. Tishin, 2010, Evolution of VTEM — Technical solutions for effective exploration: Presented at the ASEG/PESA Conference & Exhibition, Australian Society of Exploration Geophysicists/PESA, Extended Abstracts, doi:10.1071/ASEG2010ab093.

Meju, M. A., 1998, A simple method of transient electromagnetic data analysis: Geophysics, **63**, 405–410, http://dx.doi.org/10.1190/1.1444340.

Oldenburg, D. W., E. Haber, and R. Shekhtman, 2013, Three dimensional inversion of multisource time domain electromagnetic data: Geophysics, **78**, no. 1, E47–E57, http://dx.doi.org/10.1190/geo2012-0131.1.

Pidlisecky, A., K. Singha, and F. D. Day-Lewis, 2011, A distribution-based parametrization for improved tomographic imaging of solute plumes: Geophysical Journal International, **187**, no. 1, 214–224, http://dx.doi.org/10.1111/j.1365-246X.2011.05131.x.

Schenk, O., K. Gärtner, W. Fichtner, and A. Stricker, 2001, PARDISO: A high-performance serial and parallel sparse linear solver in semiconductor device simulation: Future Generation Computer Systems, **18**, no. 1, 69–78, http://dx.doi.org/10.1016/S0167-739X(00)00076-5.